SAND2015-2969J

Coupling in-situ TEM and ex-situ analysis to understand heterogeneous sodiation of antimony

*Zhi Li**, [a ‡] *Xuehai Tan*, [a ‡] *Peter Kalisvaart,* [a] *Matthew T. Janish,* [b] *William M. Mook,* [c] *Katherine L. Jungjohann*, [c] *C. Barry Carter* [b] and *David Mitlin** [d,a]

a Chemical and Materials Engineering, University of Alberta, Edmonton, Alberta T6G 2V4, Canada

b Department of Materials Science and Engineering, University of Connecticut, Storrs, CT 06269, USA

c Center for Integrated Nanotechnologies, Sandia National Laboratories, Albuquerque, NM 87185, USA

d Chemical & Biomolecular Engineering and Mechanical Engineering, 8 Clarkson Avenue, Potsdam NY 13699, USA

lizhicn@gmail.com, dmitlin@clarkson.edu

Keywords: in-situ TEM, sodium ion, lithium ion, battery, NIB, NaB, SIB, LIB

Abstract

An in-situ electrochemical cell has been used for analysis in the transmission electron microscope (TEM) together with ex-situ time-of-flight, secondary-ion mass spectrometry (TOF-SIMS) depth profiling to detail the structural and compositional changes associated with Na/Na^+ charging/discharging of 50 and 100 nm thin films of Sb. TOF-SIMS on a partially sodiated 100 nm Sb film gives a Na signal that progressively decreases towards the current collector, indicating that sodiation does not proceed uniformly. This lack of uniformity will lead to local volumetric expansion gradients that would in turn serve as a major source of intrinsic stress in the microstructure. Two mechanisms could lead to the resulting relaxation of both the intrinsic and the extrinsic (film-collector mismatch) stresses. In-situ TEM shows time-dependent buckling and separation of the sodiated films from their inactive support, i.e., the TiN-coated Ge nanowire. Failure does not occur directly at the interface, but rather at a short distance away within the Sb phase. TOF-SIMS highlights time-dependent segregation of Na within the structure, both to the film-current collector interface and to the film surface where a solid electrolyte interphase (SEI) exists. Since earlier theoretical work indicated that a progressive increase of the Na content in Sb would result in major elastic softening of the material, it is proposed that this segregation will lower the strain energy in the film and reduce its flow stress.

1. Introduction

The ever-growing energy-storage requirements for transport electrification and the large-scale smart grid have stimulated intensive research into high-efficiency energy storage technologies.[1] Among the various rechargeable battery systems, Li-ion batteries (LIBs) are the most developed and are widely used for portable electronics.[2-4] However, for large-scale applications such as in electric vehicles (EVs), there are increasing concerns about the geographically isolated distribution and the high commodity prices of lithium resources. Sodium is a promising alternative charge carrier, with a desirable redox potential (only 0.3V higher than lithium) and an almost unlimited supply from desalination of sea water.[5-7] For this reason, sodium-ion batteries (SIBs), which are also known as Na-ion batteries (NaBs or NIBs), have received tremendous scientific and engineering attention in recent years.[8-14]

A major effort for SIB research is to develop suitable anode materials. The radius of the Na ion is larger than that of Li (0.097 nm vs 0.068 nm).[5] For example, Na does not easily intercalate into graphite: it gives a very small capacity of 30-35 mAh g^{-1}.[15] Recently, a much larger storage capacity of ~300 mAh g^{-1} was achieved for sodium in carbonaceous materials that had a dilated inter-graphene spacing.[16-18] Of the possible alloying anode materials amorphous Ge has been shown to be amenable to sodiation giving a Na to Ge ratio of slightly above 1:1 (~360 mAh/g). [19-21] Crystalline Ge nanowires do not appear to accommodate Na.[7] Tin and related materials have been intensively studied for SIB applications, with a maximum theoretical capacity of 847 mAh g^{-1} ($Na_{15}Sn_4$ intermetallic). For Sn electrodes it is essential to control the nanostructure to accommodate the larger volume expansion during sodiation (~400% vs. 260% during lithiation).[22-24]

Antimony is another highly promising electrode material, giving a theoretical capacity of 660 mAh g^{-1} for both Li and Na.[25-27] Recently, composite materials based on Sb have produced promising SIB anodes; examples include Sb/carbon nanocomposites, [28-31] monodisperse Sb nanocrystals, [26] Sb hollow Nanospheres,[32] electrospun Sb/C Fibers,[33] Sb_2S_3/graphene composites.[34] Bulk Sb, [27, 35] Sb_2S_3 [36] and other Sb-based alloys [37-40] have also been explored. The expansion of Sb to the fully sodiated hexagonal ($P6_3/mmc$) Na_3Sb phase ($\Delta V/V_{pristine}$) is 293%, so major changes in the stress state of the material during charging/discharging are anticipated. Work on the cycling of pure Sb films has shown a very rapid capacity decay during cycling, indicating that there is a highly active failure mechanism.[25] Although ex-situ experiments and theoretical modeling work have been carried out to study the sodiation mechanisms in the case of Sb,[27] in-situ and operando studies on the material remain limited but will be essential for providing direct phenomenological insight into the sodiation behavior.

In-situ transmission electron microscopy (TEM) is an essential tool for obtaining insight into a range of phase transformation behaviors, including site-specific lithiation and sodiation events. [41-43] It is especially useful for studying alloying reactions (e.g., those involving Sn, Sb and Ge), where sodiation proceeds through a range of nucleation and growth events that may be tracked both chemically and crystallographically. In-situ TEM has been employed to examine the decomposition of electrolytes on electrode surfaces, [44-46] and both phase changes and the failure of various electrode materials, including Si,[47, 48] Sn,[24] SnO_2,[49-51] N-doped graphene,[52] carbon nanofibers [53] and $LiFePO_4$.[54] Some intriguing findings, such as the orientation-dependent mobility of a reaction front,[55, 56] self-limitation of reactions caused by stress,[41] anisotropic volume expansion, [57, 58] etc., may help guide the design of the next-generation high-performance electrode materials. This is the first such study on Sb, where we couple in-situ TEM with ex-situ

TOF-SIMS to provide new insight into the sodiation phenomenology in this highly promising material. A very basic materials microstructure was chosen for this study, namely, a thin film of Sb that was free of secondary phase additions such as carbon or binder.

2. Results and Discussion

During in-situ TEM electrochemical cells, the charging platforms generally protrude from the substrate providing a geometry that is electron transparent and ideal for further analysis. This is one of the reasons why materials like Si, Ge or SnO_2 nanowires are commonly employed for such studies.[41, 50, 58] To make it possible to examine polycrystalline Sb thin films, a platform consisting of three components was developed as illustrated in Figure 1a, with the details of the synthesis process being provided in the Experimental. We grew an array of single crystal (or twinned) Ge nanowires on a Si wedge, which was subsequently coated with a layer of TiN. Figure 1b shows the 25 nm ALD TiN conformal coating on the nanowires; this coating provides an electrically conductive path to the current collector. The single-crystal nanowires and the TiN coating are both known to be Na inactive.[19, 59] As expected, the final TiN-coated crystalline Ge nanowire array also shows negligible charge storage capacity (Figure S1). This setup actually provides a very general platform for investigating a variety of electrode materials in thin film form.

The active electrode material, Sb, was deposited onto the support surface using magnetron sputtering from a high purity elemental target. Two different Sb mass loadings (0.066 and 0.132 $mg.cm^{-2}$), corresponding to mean Sb film thicknesses of 50 and 100 nm, respectively, were investigated. Since sputtering is a highly directional PVD process that results in shadowing,

there was some local variation in film thicknesses. For labeling simplicity the Sb-on-TiN-on-Ge nanowire (NW) materials are referred to as 50nmSb/NW and 100nmSb/NW. These are compared to blanket Sb films that were studied in parallel, being labeled 50nmSb and 100nmSb.

Figure S2 shows the XRD pattern of the as-synthesized 100nmSb/NW. The (111), (220) and (311) reflections of Ge ($Fd\bar{3}m$ (227)), and the (111), (200) and (220) reflections of the Au catalyst used for growing the GeNWs are present. For the polycrystalline Sb film, the Bragg peaks located at $2\theta = 23.7°$, 28.7° and 40.1° are indexed as the (003), (012), and (104) reflections of the rhombohedral lattice ($R\bar{3}m$ (166)). Figure 1c and Figure S3 show representative scanning electron microscopy (SEM) images of the as-synthesized 50nmSb/NWs and 100nmSb/NWs. From the images of a single wire, it is evident that Sb wets the TiN surface quite well, forming a uniform and continuous layer on the support surface. Figure 1d shows a high-angle annular dark-field (HAADF) image of a single 50nmSb/NW, with the associated X-ray energy-dispersive spectroscopy (XEDS) line scan shown in Figure 1e. In this case the overall thickness and the morphology of the Sb film is uniform along the length scale of the wire. As will be shown, however, some wires possess a varying Sb film thickness along the circumference of the wire; the 'bottom' (relative to the sputter flux) being consequently thinner than the 'top'. This nonuniformity is distinct from the lengthwise tapered geometry of the Sb films encountered during the in-situ sodiation process.

A nanosized half-cell was assembled onto a commercial scanning tunneling microscopy (STM) TEM holder (Nanofactory Instruments), offering piezo-controlled nm-scale motion in three dimensions. On one end of the STM holder, the working electrode was mounted onto an aluminum rod using conductive epoxy. On the other end, bulk Na metal, which is the counter

electrode, was attached to a tungsten rod. All the material handling was conducted in a dry He-filled glovebox (moisture and oxygen content less than 3 ppm). The TEM holder was sealed in an He-filled plastic bag while being transferred and loaded into the TEM column. During the entire loading procedure the air exposure of the sample is approximately 5 seconds. This exposure is long enough for a thin layer of Na_2O and NaOH to form on the surface of the exposed Na metal. This reaction layer served as the ion-conducting but electrically isolating solid electrolyte in the experiments, preventing the electrochemical cell from shorting. To perform the in-situ sodiation/desodiation experiments a 4 V (vs. Na counter electrode) cathodic/anodic bias was applied to the Sb.

Figure 2 captures the real-time structural changes of 50nmSb/NW at different stages during one full sodiation-desodiation cycle. The panels show bright-field images of 50nmSb/NW during initial sodiation, followed by desodiation. The indexed selected-area diffraction (SAD) patterns are shown with the associated images. To minimize the electron-beam damage to the microstructure, we acquired images with a typical time interval of 5~10 minutes. The electron beam was always blanked, except for when the actual images were taken. For typical magnification i.e. 35k we used for imaging, the electron dose rate is 7.74 $e^-/Å^2 \cdot s$. The pristine Sb film shows a clear interface with the supporting nanowire (Figure 2a). By comparing the experimental SAD patterns with simulated patterns, it can be confirmed that the NW core is a single crystal oriented near the $[1\,\bar{1}\,0]$ zone axis and that the Sb and TiN phases are polycrystalline. In the dark-field TEM image obtained using the $\mathbf{g} = (002)_{Ge}$ reflection (Figure S4), the single crystal NW core is uniformly bright, allowing a better view of the sharp interface between NW and the TiN. The sharp interface is essential to accurately evaluate the structure changes of the Sb thin films.

Upon sodiation, the Sb film swells while the NW core and the TiN layer remain unchanged. The arrow in Figure 2b points to the direction of sodiation, which starts where the wire makes contact with the Na source at its bottom left tip. The Na source is outside the field of view, while the diffuse sodiation front is visible in the 7 and 15 minute specimens. As may be seen from the shape of Sb film, which is now tapered, sodiation is not uniform. Rather it proceeds gradually along the length of the nanowire, which leaves the initially uniform Sb film with a thickness that increases towards the Na source. The Sb film that has been sodiated for 15 minutes (Figure 2c) remains nonuniform in thickness. However after 30 minutes of sodiation (Figure 2d) the front has already passed the field of view, and the imaged sodiated Sb film becomes uniform again but now with a substantially greater thickness.

While the diffraction rings of pristine Sb progressively diminish with increasing sodiation time, there is no evidence of a new crystalline phase forming after 7 or 15 minutes of sodiation. Since the thickness of the Sb film is indeed growing, the intermediate sodiated microstructure of Na_xSb is presumably amorphous, agreeing with the detailed experimental analysis and modeling results.[27, 60] As shown in Figure 2d, after 30 minutes sodiation, the SAD pattern starts to show a new set of diffraction rings, with the inner halos being the most prominent feature. The diffraction pattern, upon further sodiation for approximately 7 hours (kept overnight), can be indexed as belonging to nanocrystalline hexagonal Na_3Sb (P63/mmc (194)) and Na_2O. It is probable that some amorphous Na_xSb remains in the system, due to the presence of an amorphous halo that overlaps with the first two Na_3Sb rings. This, combined with the proximity of the TiN and Na_2O reflections, creates some ambiguity in indexing the experimental pattern. However, as it is well established that no other crystalline Na-Sb phases are known to form during electrochemical sodiation[27, 60]. To recognize the presence of amorphous Na_xSb, the

material is referred to as “terminally sodiated” rather than “fully sodiated”. This distinction acknowledges that while little additional sodiation occurs after 7 hours, full theoretical capacity is not be reached with the in-situ geometry. It has been proven in an earlier in-situ TEM study that the stress induced by the lithiation reaction front is substantial enough to prevent a Si nanowire with a diameter larger than 40nm from fully lithiating [41]. A similar case may occur here. Even after the Sb is terminally sodiated, the underlying NW structure remains intact, which can be confirmed by the sharp interfaces in the bright field images. There is no evidence of fracture of the underlying support, indicating that the sodiation strains are confined to the active Sb phase.

The terminally sodiated film shown in Figure 2e is no longer smooth, showing instead what appears to be localized bucking and variations in mass-thickness (lighter areas in the bright field images). Moreover after being held for 7 hours, a portion of the sodiated Sb is locally delaminated. This region is arrowed in Figure 2f. This failure occurs not directly at the Sb-TiN interface, but within the film. The separation of the Sb film from the underlying support is due to the differential stresses that build up during the sodiation-induced expansion. This process appears to be time-dependent, occurring some time after the Sb has reached the terminally sodiated state.

The desodiation results are shown in Figures 2g and 2h. After 40 minutes of desodiation, the SAD pattern indicates that the Na_3Sb phase is still present, although the relative intensity of the Bragg rings relative to the amorphous-phase halo is markedly reduced. This observation indicates a two-phase transformation sequence with the intermetallic transforming back into an amorphous Sb-Na solid solution. The final desodiated film morphology shows substantial

differences from its initial state. Much of the structural damage induced during prior sodiation is irreversible, which is reasonable since there is no obvious mechanism for 'healing' the Sb film.

Figures 3a and 3b present higher-magnification images of the same area in Sb/NW before and after sodiation, in a region where the interface has not slipped. The diameter of the Ge nanowire (bottom arrow in 3a) and the thickness of TiN coating (middle arrow in 3a) are unchanged. By measuring the cross-sectional change of the Sb shell, a change in volume of 269% is calculated; this value is less than the theoretical 294% for pristine Sb to hexagonal Na_3Sb transition. [27] The difference should be due to the failure of the Sb to fully sodiate. However some (undetected) interfacial slippage may allow the Sb shell to expand longitudinally as well as radially during sodiation. Figure S5 shows a HAADF micrograph of 50nmSb/NW in the terminally sodiated state along with XEDS analysis and the corresponding bright field STEM micrograph. The results further confirm the intact structure of the Ge nanowires and of TiN.

A nanowire in the 100nmSb/NW electrode that received a significantly higher Sb loading on one of its sides versus the other has also been examined. This particular wire was aligned nearly perpendicular lengthwise to the sputter flux, resulting in notably thicker Sb coating on the "top" side. This structure allowed the mechanical damage in Sb films with different thicknesses, but at analogous sodiation/desodiation states, to be studied. Figure 4a shows an area where mechanical damage is present in the terminally sodiated state. Although some film delamination (the lighter regions) is present in the thinner film, damage is much more pronounced on the thicker side. The underlying Ge nanowire is now actually bent, being concave on the side of the thinner film. For a misfitting film on a support the strain energy is known to be linearly[61] or logarithmically[62] related to the thickness of the film. Thus a thicker Sb film that has undergone

the same level of sodiation as a thinner Sb film will exert a larger compressive force on the underlying nanowire, causing the observed bending.

The pop-up structure on the thick side of the Sb film shows a type of ruffling morphology that is caused by compressive stresses.[63-65] The pop-up does not heal during desodiation, but actually becomes more pronounced, as shown in Figures 4b – 4d. XEDS elemental mapping analysis of the area marked in Figure 4c. The Sb map is shown in Figures 4d, with the Ge and Ti and Na maps being shown in Figure S6. The combination of the Sb elemental map and the HAADF image indicates that Sb is found on both sides of the pop-up. It therefore appears that separation occurs primarily *through* the Sb film, rather than at the Sb-TiN interface. From the Ge and Ti maps, it may be concluded that the Ge core and TiN coating remain intact.

A second important observation regarding pop-up is that it locally prevents the adjacent Sb film from subsequently desodiating. This observation is confirmed by comparing the thickness of the desodiated film on the side of the pop-up facing the counter electrode, to the thickness on its opposite side. On the side of the counter electrode the thickness decreases from an initial 165 nm to 125 nm. Conversely on the other side the thickness only decreases to 160 nm. The geometry of the pop-up will reduce the effective cross-section, creating a 'traffic jam' that locally lowers the net rate of Na flux. In addition, there may be complex effects associated with a non-uniform electrical field in the damaged region that further reduces the local driving force for desodiation.

Similar failure mechanisms could be active in Sb thin film electrodes during charging/discharging of a conventional half-cell. However, it must be remembered that when the

electrodes that are submerged in the electrolyte, the sodiation front would proceed from all surfaces rather than just from the contacting tip. Computer simulations indicate that long-range strain is greater for sodiation than for lithiation of Sb [27]. This was attributed to a lower diffusivity of Na in Sb, which does not allow for as facile of stress relaxation through creep [27]. The lower diffusivity and higher strain were also proposed as an explanation for why a series of amorphous solid solutions, rather than equilibrium intermediate phases, are observed prior to reaching the terminal crystalline Na_3Sb [27]. The inability of the Sb to relax sodiation strain through uniform diffusional flow is consistent with the observed localized fracture, which is an alternative stress-relief mechanism.

To further understand the changes that occur in Sb upon sodiation, 100 nm thick Sb films on planar TiN supports (labeled 100nmSb) were cycled against metallic Na in a standard half-cell configuration, at 0.01 - 2 V; the electrolyte was 1 M $NaClO_4$ in ethylene carbonate/diethyl carbonate (1:1). Figure 5a shows the galvanostatic charge-discharge profile for the first few cycles. The cycle 1 coulombic efficiency was 82%. The reversible desodiation (charge) capacity was 623, 621 and 441 mAh/g in cycle 1, 2 and 20, respectively. The capacity versus voltage curve at cycle 1 is distinct from the subsequent cycles. Since these electrodes possess initially low surface areas (~1.5 $cm^2\ g^{-1}$), the changes in the galvanostatic profiles should not be very strongly influenced by SEI formation. The substantial difference in cycle 1 versus cycle 2 profiles (most apparent in the dQ/dV curves) may be attributed to the changes in the electrode microstructure going from as-synthesized to the desodiated state. Factors such as a reduced Sb grain size may affect dissolution/nucleation kinetics, changing positions of the derivative peaks.

From cycle 2 onwards two distinct plateaus are observed for the sodiation profile, indicating two two-phase regions, each with a distinct chemical potential. From the derived dQ/dV plot (inset in 5a), the first plateau is centered near 0.72 V with the second at 0.50 V. The capacity associated with the transition from plateau 1 to plateau 2 is approximately 200 mAh/g i.e. ~ $Na_{0.9}Sb$. These two plateaus may correspond to the phase transitions Sb + Na => amorphous $Na_{0.9}Sb$ (~200 mAh/g), and $Na_{0.9}Sb$ (amorphous) + 2 Na => Na_3Sb (with an additional 460 mAh/g). However, the time-of-flight secondary ion mass spectrometry (TOF-SIMS) results demonstrate that sodiation does not proceed uniformly through the film thickness, indicating that the phase distribution is more complex than can be inferred from the capacity of the electrode.

TOF-SIMS was used to analyze the distribution of Na along the thickness of 100nmSb that was cycled in a half-cell. Before analysis, the sample underwent a full sodiation/desodiation cycle and then was sodiated to 0.5 V (399 mAh/g, i.e., 61% of maximum capacity). The TOF-SIMS depth profiling of the Na, C, Sb, Ti and Fe are shown in Figure 5b. The x-axis shows the sputtering time, which may be qualitatively correlated to distance into the film (sputter rates may have some variation with film thickness, depending on Na content, etc.). The Sb/spacer interface can be defined at ~4000 seconds of sputtering, as indicated by the peak in the Ti profile. Since it was not possible to polish the supports to a perfect atomic flatness, the concentration depth profiles are artificially blurred near the Sb-Ti and Ti-Fe interfaces. Thus the true concentration profiles are expected to be sharper than indicated by the TOF-SIMS analysis. Based on the profile of the C and Sb signals, the SEI layer/Sb interface occurs after sputtering for 750 s and accounts for ~20% of the total film thickness. Another source for the lack of sharpness in the C profile is that C may diffuse down the hole during sputtering. Adventitious C from the chamber

would also add to this blurring. In the Sb intensity-versus-time profile, the Sb signal is detected roughly 750 s after the Na signal. This confirms the presence of SEI, which contains C and Na, but not Sb.

TOF-SIMS shows that the Na composition is not uniform across the thickness of the 400 mAh/g sodiated film. Both the Na profile and the Sb profile show changes in the relative intensity of each element as a function of sputter time. In fact there appears to be three distinct Na (and Sb) regions in the profile. First, there is a zone with high Na content. It runs from the termination of the SEI layer (20%) to approximately 30% of the film thickness (1200 s). Second, there is an intermediate Na content region, which has a decreasing slope and lasts until about 63% of the total film thickness (2500 s). Last, there is a region all the way to the TiN/Fe current collector, where the Na content rapidly decays. A variation in the Na content with the depth into the electrode is something that is feasible for a range of amorphous solid solutions, which should exist in regions one and two. Sloping Na profiles are not expected if well-defined stoichiometric intermetallics are present, as these would generate plateaus in the two-phase regions. The final region where the Na content rapidly decays may correspond to a crystalline solid solution of Na in Sb, where a large composition gradient is set up by the slow diffusivity of Na into the crystalline material and/or by the transformation stresses. A similar phenomenon was recently demonstrated for sodiation of Ge films, where the concentration profile in a polycrystalline sample was much sharper then in its amorphous counterpart.[19] An analogous sodiation profile is expected for Sb particulates, such as the ones employed in powder-based battery electrodes. A typical active phase particulate in a SIB anode may be up to tens of microns in diameter. It is expected that it would then sodiate in a radially non-uniform manner.

The above finding has a significant implication for the localized state of stress in the charging/discharging material, since the volume expansion of sodiated and lithiated alloys (e.g., Sb, Sn, Ge, Si) is effectively a rule of mixtures for the molar volume of the alloying host and of Li/Na.[66, 67] Such local composition variations will lead to very large intrinsic stresses, even if the phases are amorphous.[68, 69] This intrinsic stress will then add to the extrinsic stress that is generated due to the mismatch between the active material and the inactive current collector, and will accelerate the pulverization of the electrode during cycling. [68, 70] The in-situ TEM observation that the in-plane separation occurs within the film, rather than directly at the Sb-TiN interface, are consistent with a sodiation gradient (and hence a stress gradient) within the material. No film examined in the in-situ study fully sodiated throughout its thickness, according to both the measurements of volume expansion and the diffuse background in the SADs. Thus, failure may occur at, or near, the transition region between the Na-rich and Na-poor material where the intrinsic stresses are expected to be high.

The diffusional changes in the Na-Sb films measured by TOF-SIMS on 100nmSb specimens that were sodiated to 0.01 V were examined further. Prior to analysis the sealed half-cells cells were stored at room temperature for varying times. After being aged for 0.5 hours, 1, 3 and 7 days at room temperature, 100-nm thick Sb films on the current collector were disassembled from the coin cells and analyzed. Prior to TOF-SIMS analysis the samples were covered with Parafilm (first protection) and sealed in a zip bag (second protection) in a glove box to avoid air exposure. The airtight sample was immediately transferred to the instrument for TOF-SIMS measurement. The Na profiles are presented in Figure 5c, while the profiles of other elements are shown in Figure S7.

After 0.5 hours and 1 day, the distribution of Na is relatively uniform across the film thickness. However, after 3 days Na begins to segregate to both the film-TiN interface and the film-SEI interface. This segregation behaviour becomes more severe after 7 days of storage. Recently, researchers have modeled the sodiation of Sn, Pb and Ge and concluded that elastic softening occurs corresponding to a 75 % deterioration of the elastic moduli [71]. Additionally, plastic slippage of lithiated Si on Cu with similar thin film geometry has been both theoretically and experimentally shown to be critically linked to Li segregation and a change in bonding.[68] While much less is known about sodiated Sb, it anticipated that a similar time-dependent Na segregation will lead to analogous elastic softening, resulting in both more facile plastic deformation and a lowering of the total strain energy.

In an earlier study of sodiation versus lithiation of Sb, it was argued that since diffusion in Na-Sb is quite slow, sodiation stresses are only slowly relieved by vacancy-assisted mechanisms, and that this process is much slower than for lithiation stresses in the same material. [27] It is expected that the actual sodiation process, either in a standard half-cell or in a TEM in-situ cell, will be similar. It is already known that this process leads to amorphization of Na-Sb at the expense of the formation of intermediate phases. It now appears that an additional 'macroscopic' mechanism for release of strain energy is the time-dependent buckling, while a 'nano-scale' mechanism for reduction of strain-energy is the time-dependent sodium segregation.

3. Conclusions

In summary in-situ TEM and ex-situ TOF SIMS analysis have been used to provide information on time-dependent structural and compositional changes in nm-scale Sb thin films during

sodiation. These changes presumably act to relax the major intrinsic and extrinsic sodiation-induced stresses in the material.

Experimental Section

In-situ electrode synthesis:

To facilitate the in-situ TEM study of the electrochemical sodiation process of Sb, a nanowire support that is inert to electrochemical sodiation was designed and synthesized. Ge nanowire (GeNWs) arrays were prepared using a gold-catalyzed, vapor-liquid-solid (VLS) growth on a Si wedge (Hysitron, Inc,). A 5-nm Au catalyst layer was magnetron sputtered (AJA International, Orion) onto the top side of Si wedges at room temperature. The GeNWs array was then synthesized using a commercial chemical vapor deposition (CVD) reactor (Tystar Inc.). A 25-nm thick titanium nitride (TiN) film was then conformally coated onto the GeNWs-Si wedge assembly using atomic layer deposition (ALD) (FlexAL, Oxford Instruments). The deposition was performed at 300 °C using $TiCl_4$ and H_2/N_2 as precursor and plasma gas, respectively. This procedure provides an electrical conductive surface layer that is Na inactive. Sb deposition onto the support surface was carried out using magnetron sputtering from high-purity elemental target. All depositions were conducted at room temperature with the substrate being continuously rotated. Argon gas (purity of 99.999%) was used at a working pressure of 5×10^{-3} mbar, with a maximum base vacuum of 3×10^{-8} mbar. The sputtering rate was accurately measured in-situ using a crystal monitor at the substrate plane. The resulting structure was used as the working electrode for the in-situ TEM open-cell experiment.

Ex-situ electrochemical battery testing:

For ex-situ electrochemical testing and microstructural characterizations, mirror-polished (to 50 nm), 316 stainless steel, spacer disks (MTI corporation), with a diameter and thickness of 15.8 mm and 0.5 mm, respectively, were used as the substrates for Sb thin film deposition. Prior to Sb deposition, the spacer disks were coated with a 25 nm TiN film by ALD to mimic the exact surface condition that is used for in-situ work. The spacers were weighed after each deposition step using a high accuracy microbalance (1 μg accuracy; MX5, Mettler Toledo) to calculate the Sb mass loading. For ex-situ analysis, the thickness of each Sb film was fixed at 100 nm, unless otherwise stated. The Sb electrode, along with a polyethene separator, the electrolytes, Na foil counter electrode and electrolytes (1 M $NaClO_4$ in ethylene carbonate/diethyl carbonate) were assembled in an argon-filled glovebox into coin cells (CR2032-type) for future test. Galvanostatic charge-discharge cycling was performed using a multichannel-current static system (BT2000, Arbin Instruments, TX).

Microstructural characterization:

Scanning electron microscopy (SEM) analysis was performed on an S-4800 field emission SEM (Hitachi, Clarksburg, MD) operated at 15 kV. X-ray diffraction (XRD) analysis was performed on an AXS diffractometer (Discover 8, Bruker, Madison, WI) using a Cu-K_α radiation (λ = 1.5406 Å) that was monochromatized using a single Gobel mirror. The diffractometer was equipped with a Histar general-area two-dimensional detection system (GADDs) with a sample-detector distance of 15 cm. Conventional bright-field, dark-field, high-angle annular-dark-field (HAADF) imaging, selected-area diffraction (SAD) analysis, and X-ray energy dispersive spectroscopy (XEDS) were conducted on an FEI Tecnai G2 F30 TEM (FEI, Hillsboro, OR)

operating at 300 keV, equipped with an EDAX ECON 30 mm2 SiLi detector with a Super Ultra-Thin Window and Gatan Imaging Filter Tridiem (Gatan, Pleasanton, CA). CrystalDiffract™ and Diffraction-Ring-Profiler (Mitlin group free on-line shareware) were used to simulate electron diffraction patterns. Depth profile analysis was performed using TOF-SIMS (ION-TOF GmbH, Münster), under ultrahigh vacuum (10^{-9} mbar). 2kV Cs ions with current of ~148 nA were used for sputtering over an area of 300 × 300 μm^2 and a 25 kV A Bi-ion source was used for analysis over an area of 40 × 40 μm^2.

Author Contributions

‡These authors (ZL and XHT) contributed equally.

Funding Sources

This work was performed, in part, at the Center for Integrated Nanotechnologies, an office of Science User Facility operated for the U.S. Department of Energy (DOE) Office of Science. Sandia National Laboratories is a multi-program laboratory managed and operated by Sandia Corporation, a wholly owned subsidiary of Lockheed Martin Corporation, for the U.S. Department of Energy's National Nuclear Security Administration under contract DE-AC04-94AL85000.

References

1. Liu, J. *Adv. Funct. Mater.* **2013,** 23, (8), 924-928.
2. Goodenough, J. B.; Park, K.-S. *J. Am. Chem. Soc.* **2013,** 135, (4), 1167-1176.

3. Liu, J.; Li, N.; Goodman, M. D.; Zhang, H. G.; Epstein, E. S.; Huang, B.; Pan, Z.; Kim, J.; Choi, J. H.; Huang, X.; Liu, J.; Hsia, K. J.; Dillon, S. J.; Braun, P. V. *ACS Nano* **2015,** 9, (2), 1985-1994.
4. Yao, Y.; Liu, N.; McDowell, M. T.; Pasta, M.; Cui, Y. *Energy Environ. Sci.* **2012,** 5, (7), 7927-7930.
5. Hong, S. Y.; Kim, Y.; Park, Y.; Choi, A.; Choi, N.-S.; Lee, K. T. *Energy Environ. Sci.* **2013,** 6, (7), 2067-2081.
6. Zhou, T.; Pang, W. K.; Zhang, C.; Yang, J.; Chen, Z.; Liu, H. K.; Guo, Z. *ACS Nano* **2014,** 8, (8), 8323-8333.
7. Saubanere, M.; Ben Yahia, M.; Lebegue, S.; Doublet, M. L. *Nature Communications* **2014,** 5.
8. Oh, S.-M.; Myung, S.-T.; Yoon, C. S.; Lu, J.; Hassoun, J.; Scrosati, B.; Amine, K.; Sun, Y.-K. *Nano Lett.* **2014,** 14, (3), 1620-1626.
9. Yu, X.; Pan, H.; Wan, W.; Ma, C.; Bai, J.; Meng, Q.; Ehrlich, S. N.; Hu, Y.-S.; Yang, X.-Q. *Nano Lett.* **2013,** 13, (10), 4721-4727.
10. Lacey, S. D.; Wan, J.; Cresce, A.; Russell, S. M.; Dai, J.; Bao, W.; Xu, K.; Hu, L. *Nano Lett.* **2015,** 15, (2), 1018-24.
11. Wessells, C. D.; Peddada, S. V.; Huggins, R. A.; Cui, Y. *Nano Lett.* **2011,** 11, (12), 5421-5425.
12. Lee, H.-W.; Wang, R. Y.; Pasta, M.; Lee, S. W.; Liu, N.; Cui, Y. *Nature Communications* **2014,** 5.
13. Barpanda, P.; Oyama, G.; Nishimura, S.-i.; Chung, S.-C.; Yamada, A. *Nature Communications* **2014,** 5.
14. He, K.; Zhou, Y.; Gao, P.; Wang, L.; Pereira, N.; Amatucci, G. G.; Nam, K.-W.; Yang, X.-Q.; Zhu, Y.; Wang, F.; Su, D. *ACS Nano* **2014,** 8, (7), 7251-7259.
15. Ge, P.; Fouletier, M. *Solid State Ionics* **1988,** 28–30, Part 2, (0), 1172-1175.
16. Wen, Y.; He, K.; Zhu, Y.; Han, F.; Xu, Y.; Matsuda, I.; Ishii, Y.; Cumings, J.; Wang, C. *Nat Commun* **2014,** 5.
17. Ding, J.; Wang, H.; Li, Z.; Kohandehghan, A.; Cui, K.; Xu, Z.; Zahiri, B.; Tan, X.; Lotfabad, E. M.; Olsen, B. C.; Mitlin, D. *ACS Nano* **2013,** 7, (12), 11004-15.
18. Komaba, S.; Murata, W.; Ishikawa, T.; Yabuuchi, N.; Ozeki, T.; Nakayama, T.; Ogata, A.; Gotoh, K.; Fujiwara, K. *Adv. Funct. Mater.* **2011,** 21, (20), 3859-3867.
19. Kohandehghan, A.; Cui, K.; Kupsta, M.; Ding, J.; Memarzadeh Lotfabad, E.; Kalisvaart, W. P.; Mitlin, D. *Nano Lett.* **2014,** 14, (10), 5873-5882.
20. Abel, P. R.; Lin, Y.-M.; de Souza, T.; Chou, C.-Y.; Gupta, A.; Goodenough, J. B.; Hwang, G. S.; Heller, A.; Mullins, C. B. *J. Phys. Chem. C* **2013,** 117, (37), 18885-18890.
21. Baggetto, L.; Keum, J. K.; Browning, J. F.; Veith, G. M. *Electrochem. Commun.* **2013,** 34, (0), 41-44.
22. Liu, Y.; Xu, Y.; Zhu, Y.; Culver, J. N.; Lundgren, C. A.; Xu, K.; Wang, C. *ACS Nano* **2013,** 7, (4), 3627-3634.
23. Zhu, H.; Jia, Z.; Chen, Y.; Weadock, N.; Wan, J.; Vaaland, O.; Han, X.; Li, T.; Hu, L. *Nano Lett.* **2013,** 13, (7), 3093-3100.
24. Wang, J. W.; Liu, X. H.; Mao, S. X.; Huang, J. Y. *Nano Lett.* **2012,** 12, (11), 5897-5902.
25. Farbod, B.; Cui, K.; Kalisvaart, W. P.; Kupsta, M.; Zahiri, B.; Kohandehghan, A.; Lotfabad, E. M.; Li, Z.; Luber, E. J.; Mitlin, D. *ACS Nano* **2014,** 8, (5), 4415-29.

26. He, M.; Kravchyk, K.; Walter, M.; Kovalenko, M. V. *Nano Lett.* **2014,** 14, (3), 1255-1262.
27. Baggetto, L.; Ganesh, P.; Sun, C.-N.; Meisner, R. A.; Zawodzinski, T. A.; Veith, G. M. *J. Mater. Chem. A* **2013,** 1, (27), 7985-7994.
28. Qian, J. F.; Chen, Y.; Wu, L.; Cao, Y. L.; Ai, X. P.; Yang, H. X. *Chem. Commun.* **2012,** 48, (56), 7070-7072.
29. Ko, Y. N.; Kang, Y. C. *Chem. Commun.* **2014,** 50, (82), 12322-12324.
30. Zhou, X.; Zhong, Y.; Yang, M.; Hu, M.; Wei, J.; Zhou, Z. *Chem. Commun.* **2014,** 50, (85), 12888-12891.
31. Zhang, Y.; Xie, J.; Zhu, T.; Cao, G.; Zhao, X.; Zhang, S. *J. Power Sources* **2014,** 247, (0), 204-212.
32. Hou, H.; Jing, M.; Yang, Y.; Zhu, Y.; Fang, L.; Song, W.; Pan, C.; Yang, X.; Ji, X. *ACS Appl. Mater. Interfaces* **2014,** 6, (18), 16189-16196.
33. Zhu, Y.; Han, X.; Xu, Y.; Liu, Y.; Zheng, S.; Xu, K.; Hu, L.; Wang, C. *ACS Nano* **2013,** 7, (7), 6378-6386.
34. Yu, D. Y. W.; Prikhodchenko, P. V.; Mason, C. W.; Batabyal, S. K.; Gun, J.; Sladkevich, S.; Medvedev, A. G.; Lev, O. *Nat Commun* **2013,** 4.
35. Darwiche, A.; Marino, C.; Sougrati, M. T.; Fraisse, B.; Stievano, L.; Monconduit, L. *J. Am. Chem. Soc.* **2012,** 134, (51), 20805-20811.
36. Yu, D. Y. W.; Hoster, H. E.; Batabyal, S. K. *Sci. Rep.* **2014,** 4.
37. Baggetto, L.; Allcorn, E.; Manthiram, A.; Veith, G. M. *Electrochem. Commun.* **2013,** 27, (0), 168-171.
38. Baggetto, L.; Marszewski, M.; Górka, J.; Jaroniec, M.; Veith, G. M. *J. Power Sources* **2013,** 243, (0), 699-705.
39. Baggetto, L.; Hah, H.-Y.; Johnson, C. E.; Bridges, C. A.; Johnson, J. A.; Veith, G. M. *Phys. Chem. Chem. Phys.* **2014,** 16, (20), 9538-9545.
40. Nam, D.-H.; Hong, K.-S.; Lim, S.-J.; Kwon, H.-S. *J. Power Sources* **2014,** 247, (0), 423-427.
41. Wang, L.; Liu, D.; Yang, S.; Tian, X.; Zhang, G.; Wang, W.; Wang, E.; Xu, Z.; Bai, X. *ACS Nano* **2014,** 8, (8), 8249-8254.
42. Liang, W.; Hong, L.; Yang, H.; Fan, F.; Liu, Y.; Li, H.; Li, J.; Huang, J. Y.; Chen, L.-Q.; Zhu, T.; Zhang, S. *Nano Lett.* **2013,** 13, (11), 5212-5217.
43. Liang, W.; Yang, H.; Fan, F.; Liu, Y.; Liu, X. H.; Huang, J. Y.; Zhu, T.; Zhang, S. *ACS Nano* **2013,** 7, (4), 3427-3433.
44. Abellan, P.; Mehdi, B. L.; Parent, L. R.; Gu, M.; Park, C.; Xu, W.; Zhang, Y.; Arslan, I.; Zhang, J.-G.; Wang, C.-M.; Evans, J. E.; Browning, N. D. *Nano Lett.* **2014,** 14, (3), 1293-1299.
45. Zeng, Z.; Liang, W.-I.; Liao, H.-G.; Xin, H. L.; Chu, Y.-H.; Zheng, H. *Nano Lett.* **2014,** 14, (4), 1745-1750.
46. Sacci, R. L.; Black, J. M.; Balke, N.; Dudney, N. J.; More, K. L.; Unocic, R. R. *Nano Lett.* **2015,** 15, (3), 2011-2018.
47. Bogart, T. D.; Oka, D.; Lu, X.; Gu, M.; Wang, C.; Korgel, B. A. *ACS Nano* **2013,** 8, (1), 915-922.
48. Liu, X. H.; Zhong, L.; Huang, S.; Mao, S. X.; Zhu, T.; Huang, J. Y. *ACS Nano* **2012,** 6, (2), 1522-1531.
49. Gu, M.; Kushima, A.; Shao, Y.; Zhang, J.-G.; Liu, J.; Browning, N. D.; Li, J.; Wang, C. *Nano Lett.* **2013,** 13, (11), 5203-5211.

50. Huang, J. Y.; Zhong, L.; Wang, C. M.; Sullivan, J. P.; Xu, W.; Zhang, L. Q.; Mao, S. X.; Hudak, N. S.; Liu, X. H.; Subramanian, A.; Fan, H.; Qi, L.; Kushima, A.; Li, J. *Science* **2010,** 330, (6010), 1515-1520.
51. Nie, A.; Gan, L.-Y.; Cheng, Y.; Asayesh-Ardakani, H.; Li, Q.; Dong, C.; Tao, R.; Mashayek, F.; Wang, H.-T.; Schwingenschlögl, U.; Klie, R. F.; Yassar, R. S. *ACS Nano* **2013,** 7, (7), 6203-6211.
52. Wang, X.; Weng, Q.; Liu, X.; Wang, X.; Tang, D.-M.; Tian, W.; Zhang, C.; Yi, W.; Liu, D.; Bando, Y.; Golberg, D. *Nano Lett.* **2014,** 14, (3), 1164-1171.
53. Liu, Y.; Fan, F.; Wang, J.; Liu, Y.; Chen, H.; Jungjohann, K. L.; Xu, Y.; Zhu, Y.; Bigio, D.; Zhu, T.; Wang, C. *Nano Lett.* **2014,** 14, (6), 3445-3452.
54. Niu, J.; Kushima, A.; Qian, X.; Qi, L.; Xiang, K.; Chiang, Y.-M.; Li, J. *Nano Lett.* **2014,** 14, (7), 4005-4010.
55. Gu, M.; Li, Y.; Li, X.; Hu, S.; Zhang, X.; Xu, W.; Thevuthasan, S.; Baer, D. R.; Zhang, J.-G.; Liu, J.; Wang, C. *ACS Nano* **2012,** 6, (9), 8439-8447.
56. Yang, H.; Huang, S.; Huang, X.; Fan, F.; Liang, W.; Liu, X. H.; Chen, L.-Q.; Huang, J. Y.; Li, J.; Zhu, T.; Zhang, S. *Nano Lett.* **2012,** 12, (4), 1953-1958.
57. Yuk, J. M.; Seo, H. K.; Choi, J. W.; Lee, J. Y. *ACS Nano* **2014,** 8, (7), 7478-7485.
58. Liu, X. H.; Zheng, H.; Zhong, L.; Huang, S.; Karki, K.; Zhang, L. Q.; Liu, Y.; Kushima, A.; Liang, W. T.; Wang, J. W.; Cho, J.-H.; Epstein, E.; Dayeh, S. A.; Picraux, S. T.; Zhu, T.; Li, J.; Sullivan, J. P.; Cumings, J.; Wang, C.; Mao, S. X.; Ye, Z. Z.; Zhang, S.; Huang, J. Y. *Nano Lett.* **2011,** 11, (8), 3312-3318.
59. Memarzadeh, E. L.; Kalisvaart, W. P.; Kohandehghan, A.; Zahiri, B.; Holt, C. M. B.; Mitlin, D. *J. Mater. Chem.* **2012,** 22, (14), 6655-6668.
60. Baggetto, L.; Hah, H.-Y.; Jumas, J.-C.; Johnson, C. E.; Johnson, J. A.; Keum, J. K.; Bridges, C. A.; Veith, G. M. *J. Power Sources* **2014,** 267, (0), 329-336.
61. Mitlin, D.; Misra, A.; Radmilovic, V.; Nastasi, M.; Hoagland, R.; Embury, D. J.; Hirth, J. P.; Mitchell, T. E. *Philos. Mag.* **2004,** 84, (7), 719-736.
62. Mitlin *, D.; Misra, A.; Mitchell, T. E.; Hirth, J. P.; Hoagland, R. G. *Philos. Mag.* **2005,** 85, (28), 3379-3392.
63. Ohring, M., Chapter 9 - Film structure. In *Materials Science of Thin Films (Second Edition)*, Ohring, M., Ed. Academic Press: San Diego, 2002; pp 495-558.
64. Kornev, K. G.; Srolovitz, D. J. *Appl. Phys. Lett.* **2004,** 85, (13), 2487-2489.
65. Greene, J. E., Chapter 12 - Thin Film Nucleation, Growth, and Microstructural Evolution: An Atomic Scale View. In *Handbook of Deposition Technologies for Films and Coatings (Third Edition)*, Martin, P. M., Ed. William Andrew Publishing: Boston, 2010; pp 554-620.
66. Al-Maghrabi, M. A.; Thorne, J. S.; Sanderson, R. J.; Byers, J. N.; Dahn, J. R.; Dunlap, R. A. *J. Electrochem. Soc.* **2012,** 159, (6), A711-A719.
67. Todd, A. D. W.; Ferguson, P. P.; Fleischauer, M. D.; Dahn, J. R. *International Journal of Energy Research* **2010,** 34, (6), 535-555.
68. Stournara, M. E.; Xiao, X.; Qi, Y.; Johari, P.; Lu, P.; Sheldon, B. W.; Gao, H.; Shenoy, V. B. *Nano Lett.* **2013,** 13, (10), 4759-4768.
69. Sheldon, B. W.; Soni, S. K.; Xiao, X.; Qi, Y. *Electrochem. Solid-State Lett.* **2011,** 15, (1), A9-A11.
70. Li, X.; Gu, M.; Hu, S.; Kennard, R.; Yan, P.; Chen, X.; Wang, C.; Sailor, M. J.; Zhang, J.-G.; Liu, J. *Nat Commun* **2014,** 5.

71. Mortazavi, M.; Deng, J.; Shenoy, V. B.; Medhekar, N. V. *J. Power Sources* **2013,** 225, (0), 207-214.

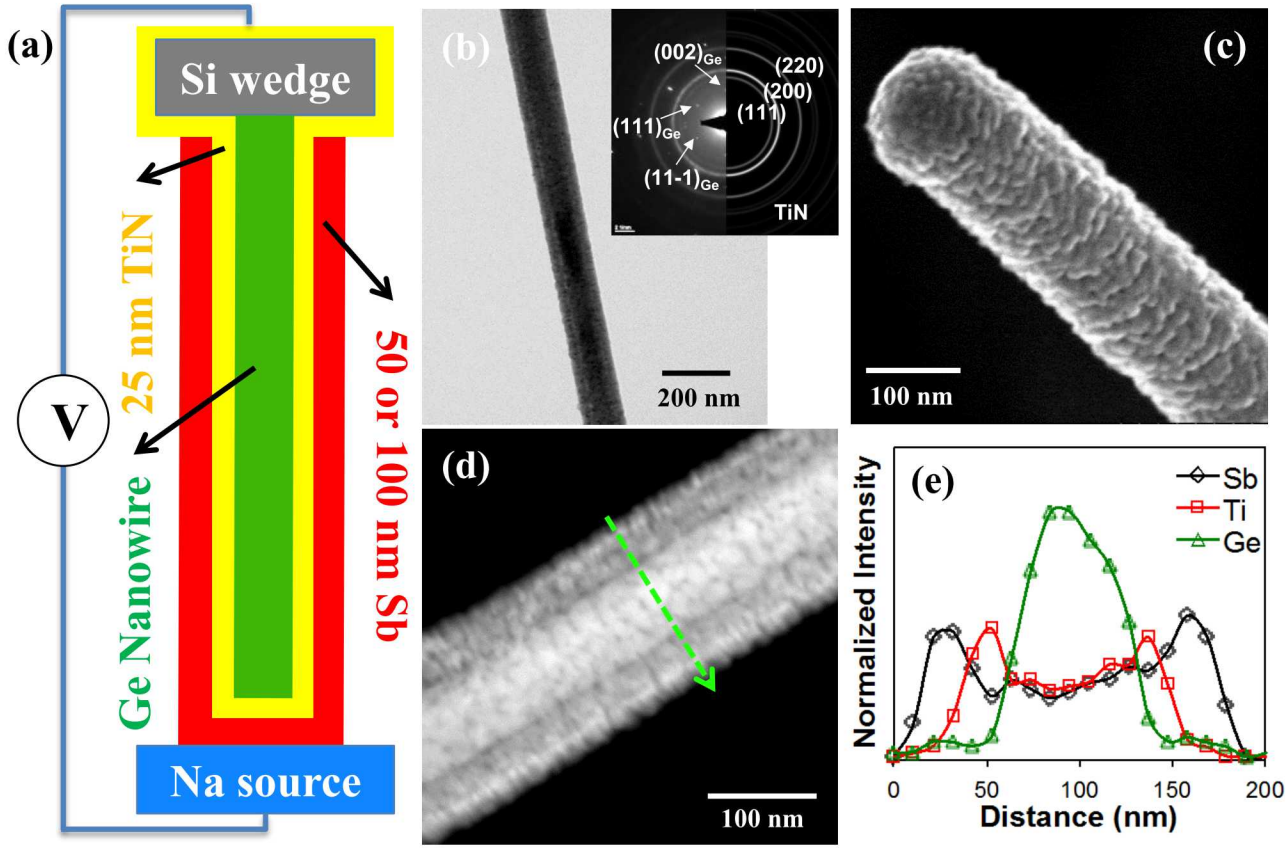

Figure 1: (a) Illustration for the setup of the in-situ transmission electron microscopy (TEM) open-cell experiment. (b) Bright field TEM micrograph of a single TiN coated Ge nanowire, with the associated indexed (polycrystalline TiN and single crystal Ge) selected area diffraction pattern being inserted. (c) SEM micrograph of 50 nm Sb on TiN/Ge nanowire, hereafter labeled as 50nmSb/NW. The Sb film fully wets the TiN surface. (d) and (e) HAADF micrograph and XEDS line scan for 50nmSb/NW.

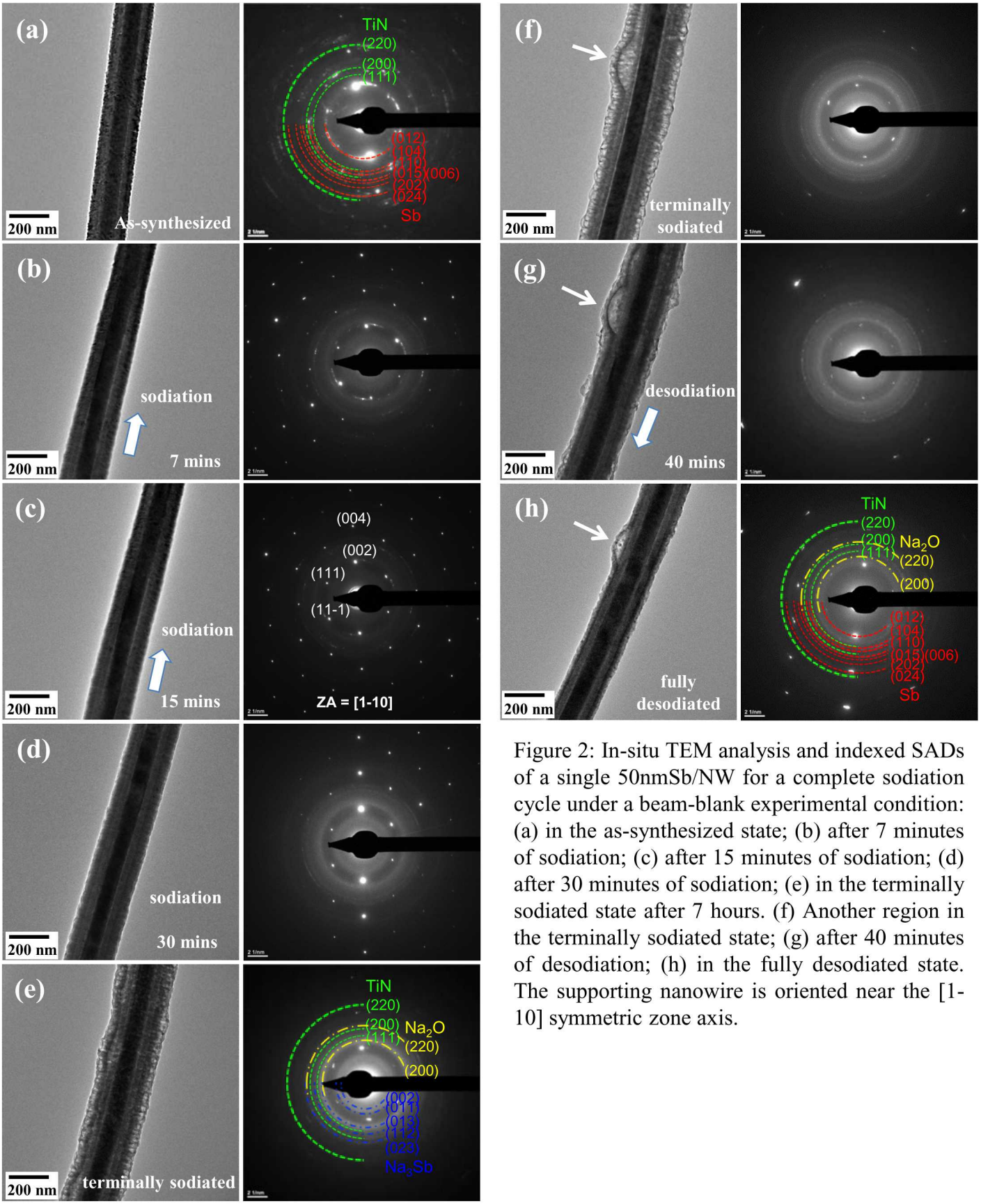

Figure 2: In-situ TEM analysis and indexed SADs of a single 50nmSb/NW for a complete sodiation cycle under a beam-blank experimental condition: (a) in the as-synthesized state; (b) after 7 minutes of sodiation; (c) after 15 minutes of sodiation; (d) after 30 minutes of sodiation; (e) in the terminally sodiated state after 7 hours. (f) Another region in the terminally sodiated state; (g) after 40 minutes of desodiation; (h) in the fully desodiated state. The supporting nanowire is oriented near the [1-10] symmetric zone axis.

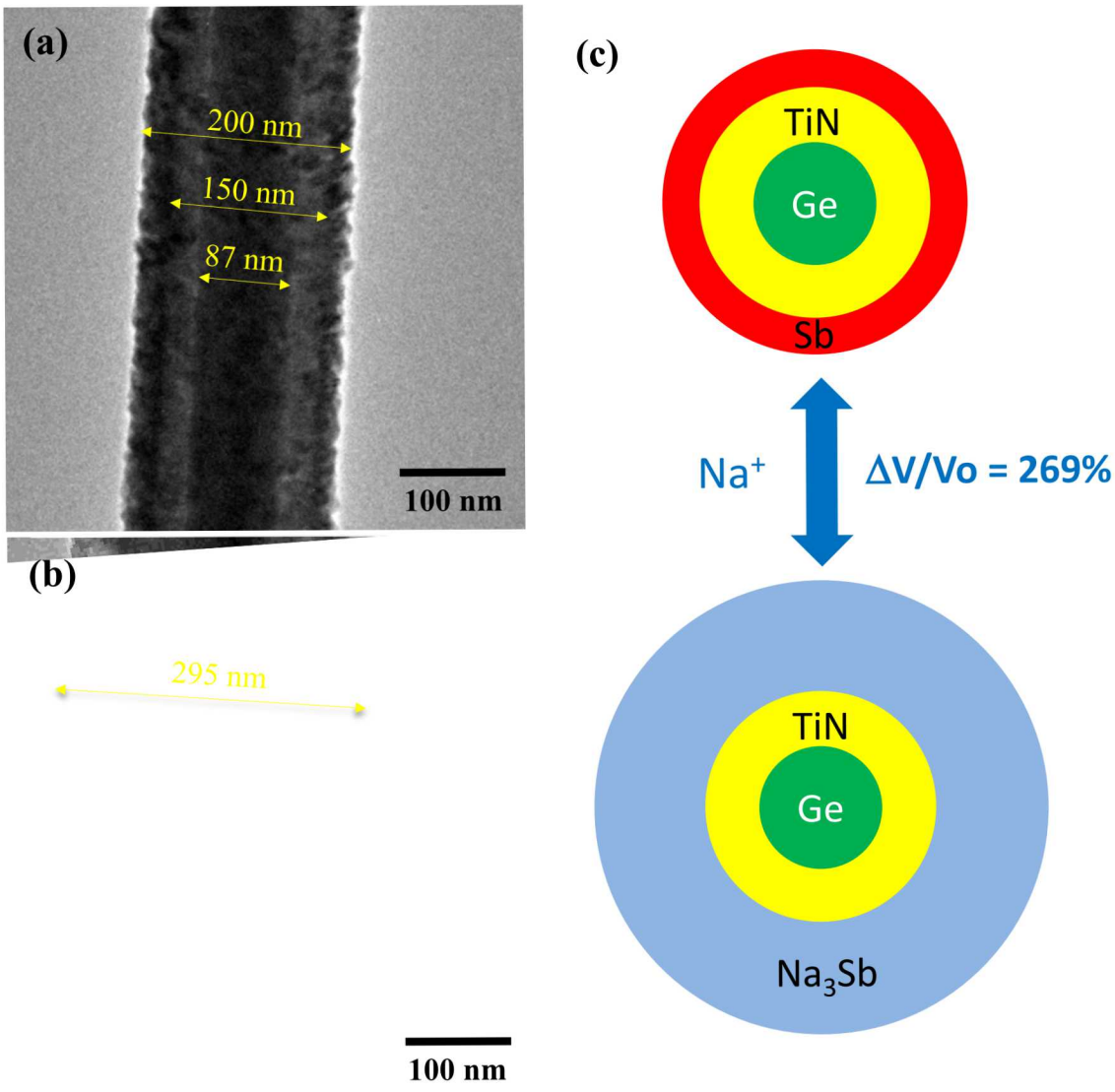

Figure 3. TEM micrographs for the same portion of nanowire before (a) and after (b) sodiation, where the thickness change of Sb layer is shown. (c) schematic illustration of the cross-sectional changes of the nanowire based on the data obtained in (a) and (b).

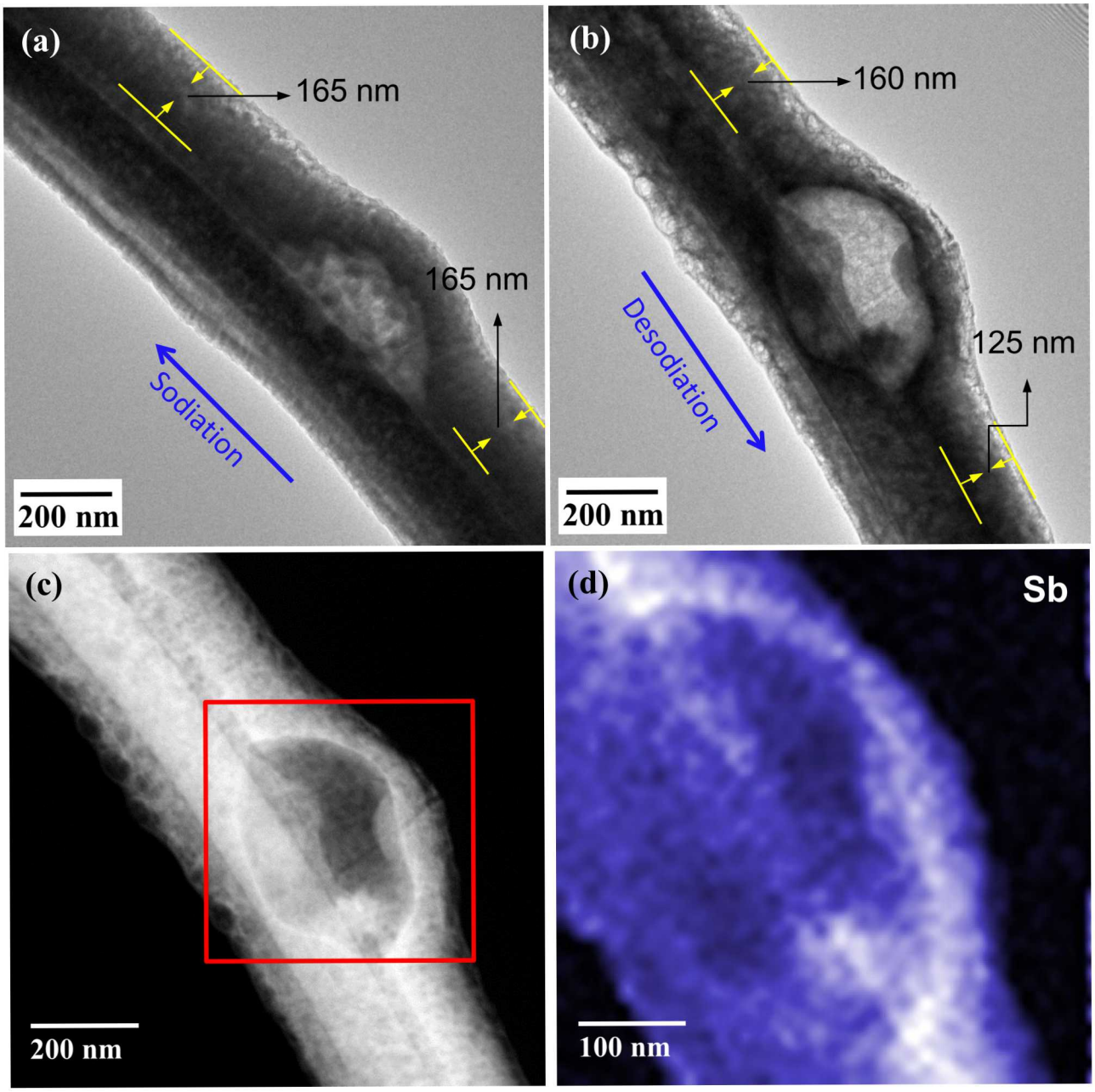

Figure 4: In-situ TEM analysis of a single 100nmSb/NW for a complete sodiation-desodiation cycle. (a) In the terminally sodiated state, after being held for approximately 10 hours (left overnight); (b) in the desodiated state. (c, d) The corresponding HAADF micrographs and XEDS elemental map of Sb in the desodiated state.

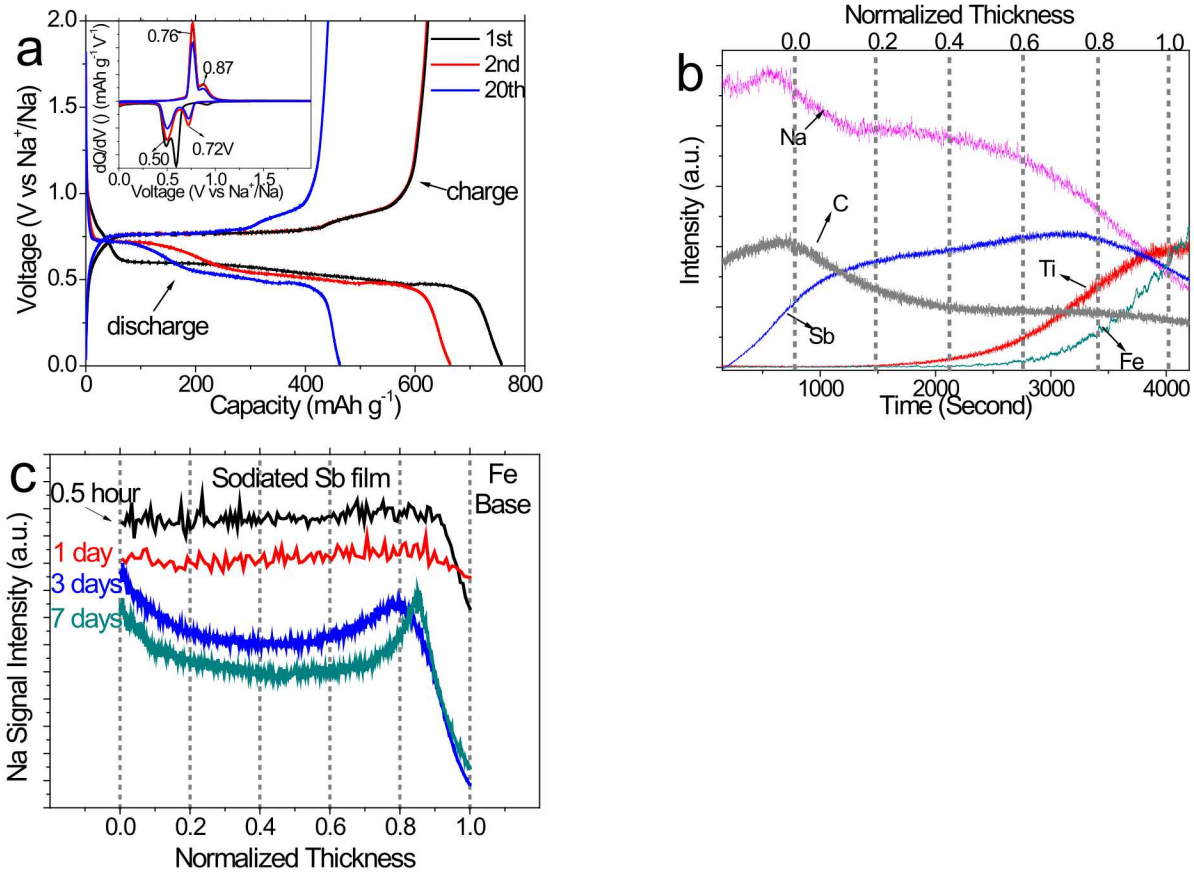

Figure 5: (a) Galvanostatic charge/discharge curves of 100 nm Sb blanket film "100nmSb" in a half-cell configuration against Na, cycled between 0.01 and 2 V at 50mA g^{-1}, with inset showing dQ/dV vs. V. (b) TOF-SIMS depth profiles through 100nmSb that was fully sodiated/desodiated once, and then partially sodiated to 0.5 V (450 mAh/g, $Na_{2.1}Sb$). (c) TOF-SIMS depth profiles of the Na signal across fully sodiated 100nmSb. Samples were stored at room temperature (sealed coin cells) for 0.5 hours, 1, 3 and 7 days prior to analysis.

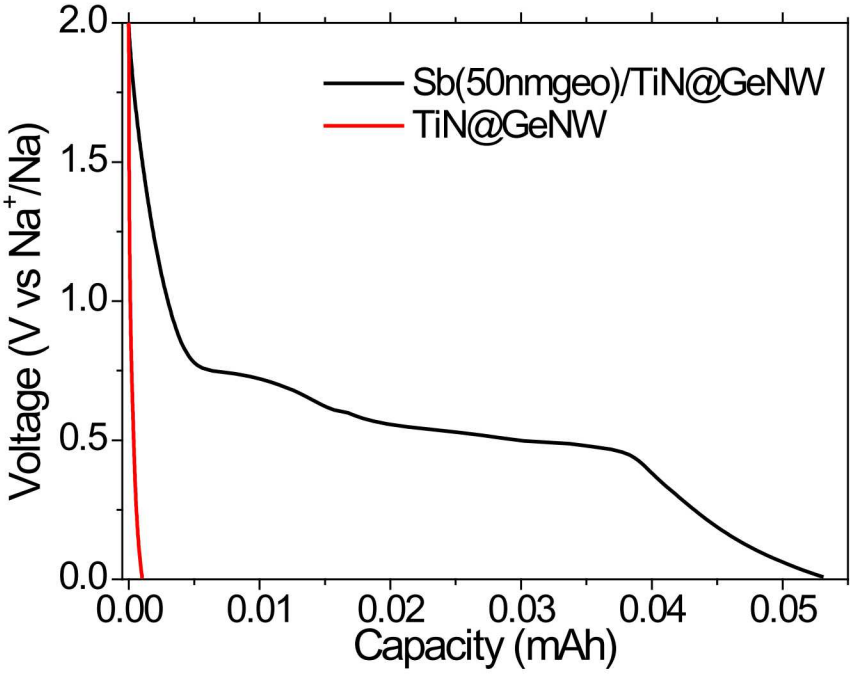

Figure S1: The 2nd cycle discharge curve of Sb(50nm geo)/TiN@GeNW in comparison with the baseline TiN@GeNW (25 nm TiN coated Ge nanowire array) in a half-cell configuration against Na, tested between 0.01 and 2V.

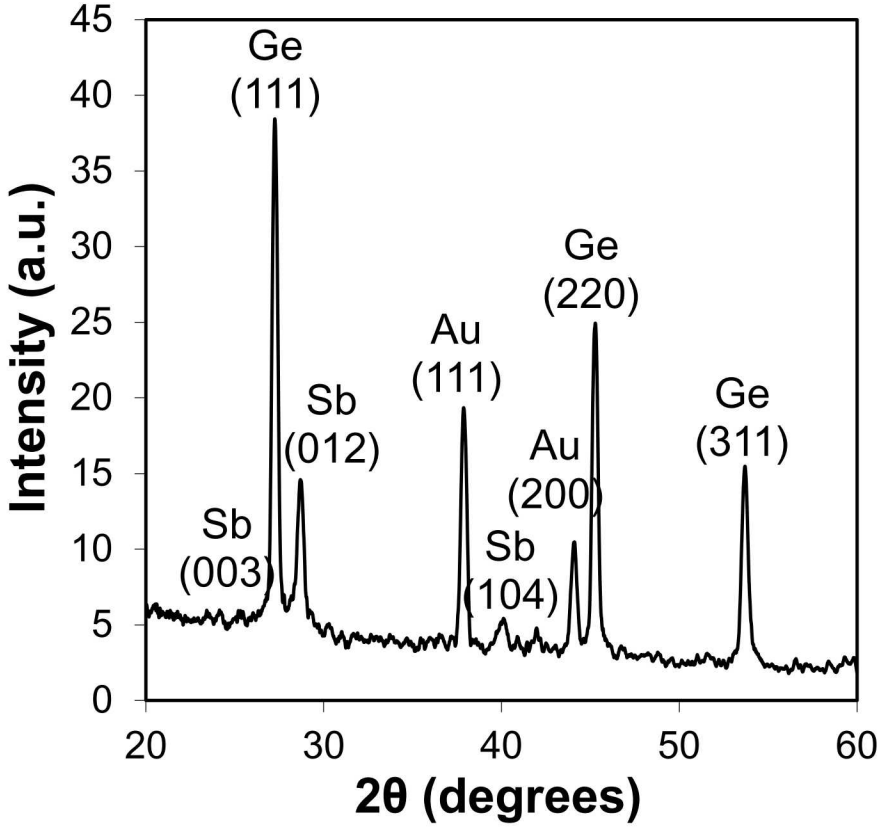

Figure S2: X-ray diffraction pattern of 100nmSb/NW.

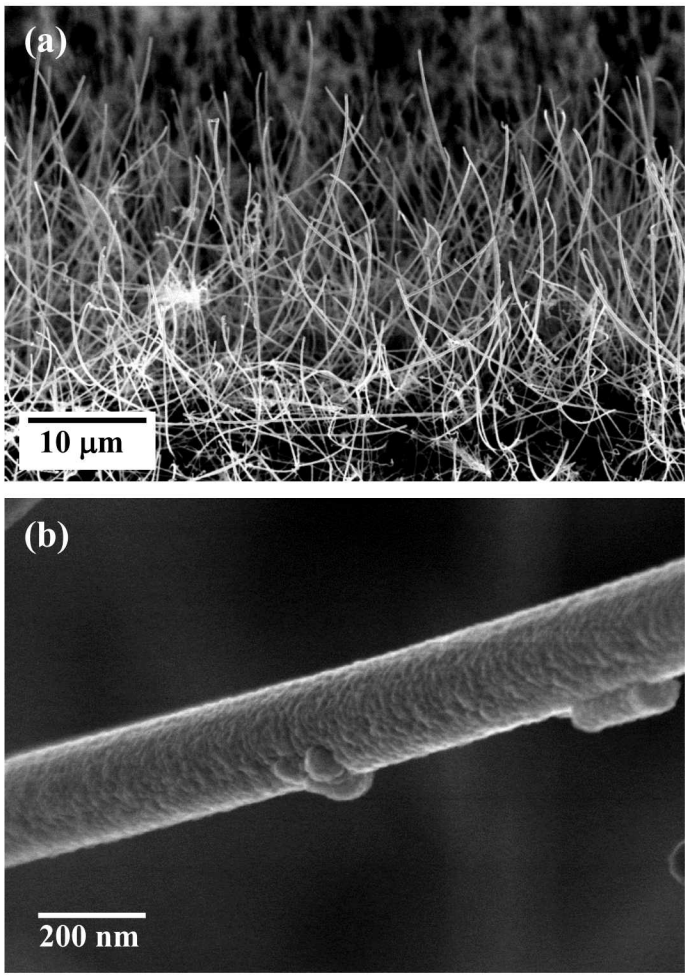

Figure S3. (a) Low and (b) high magnification SEM micrographs of the as-synthesized 100nmSb/NWs

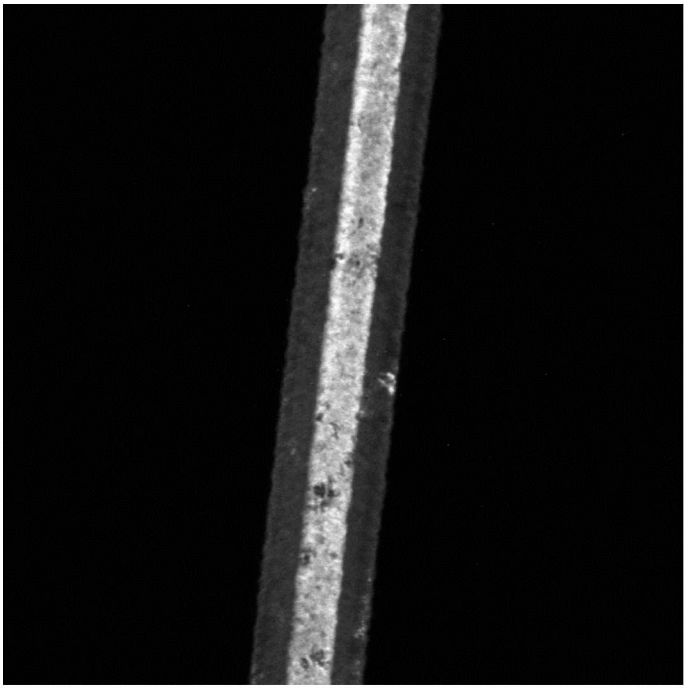

Figure S4. Dark field TEM micrograph of the 50nmSb/NW shown in Figure 2a, obtained using g = (002)Ge reflection.

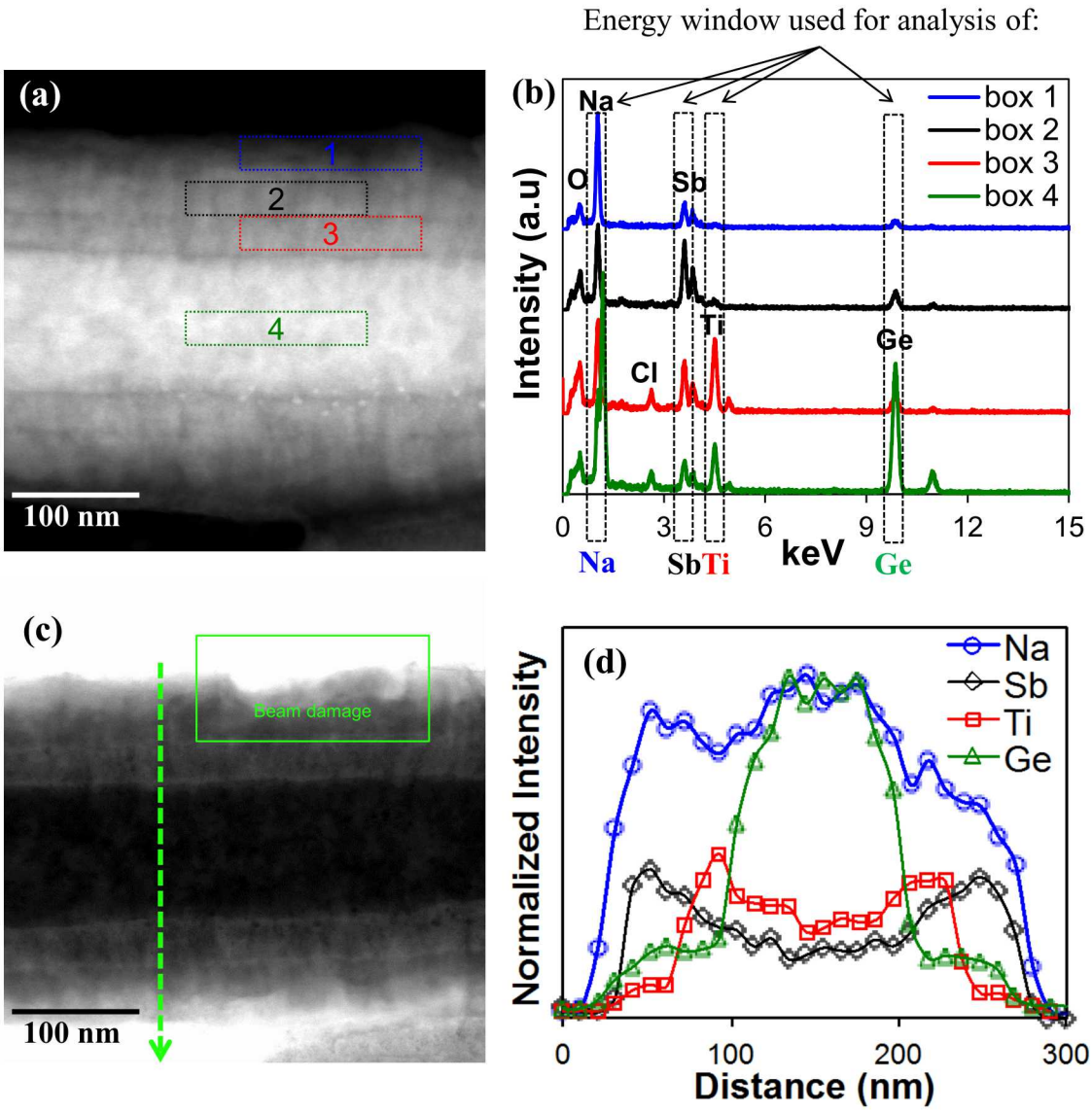

Figure S5. (a) HAADF micrograph of 50nmSb/NW in the fully sodiated state. (b) XEDS analysis of the region boxes marked in (a). (c) The corresponding BF-STEM micrograph highlights the beam damage after XEDS analysis in region 1. (d) The XEDS analysis along the arrow shown in (c). These results confirm GeNW core-TiN interlayer-Sb shell coaxial structure after sodiation, as TiN-coated crystalline Ge nanowire support is supposed to be Na inactive.

The energy windows shown with the XEDS spectra (see Figure S5b) indicate the corresponding energy window that was used to generate the line profile and the elemental map for each element. For certain elements, there is partial energy overlapping that can not be avoided while doing the analysis. For example, the Na signal actually follows the signal of Ge. This is caused by the energy overlapping between the Na Kα line and Ge Lα line.

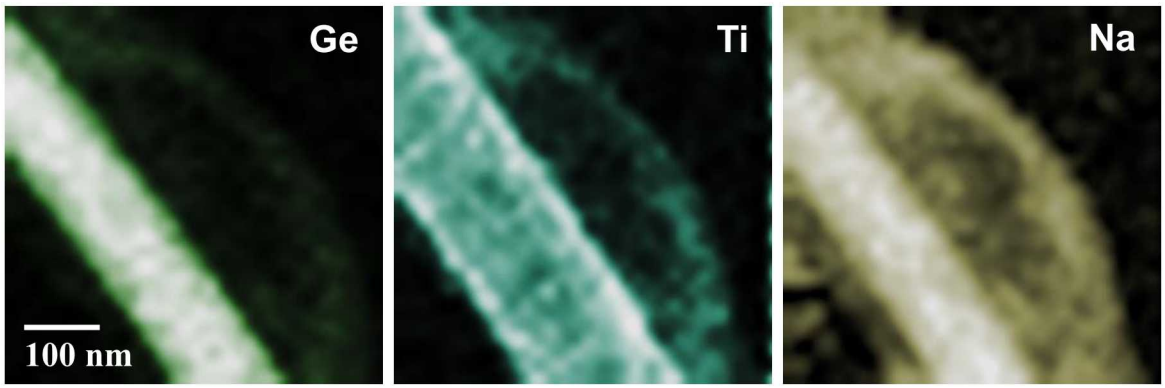

Figure S6: The corresponding XEDS elemental maps of Ge, Ti and Na for the 100nmSb/NW shown in Figure 4c.

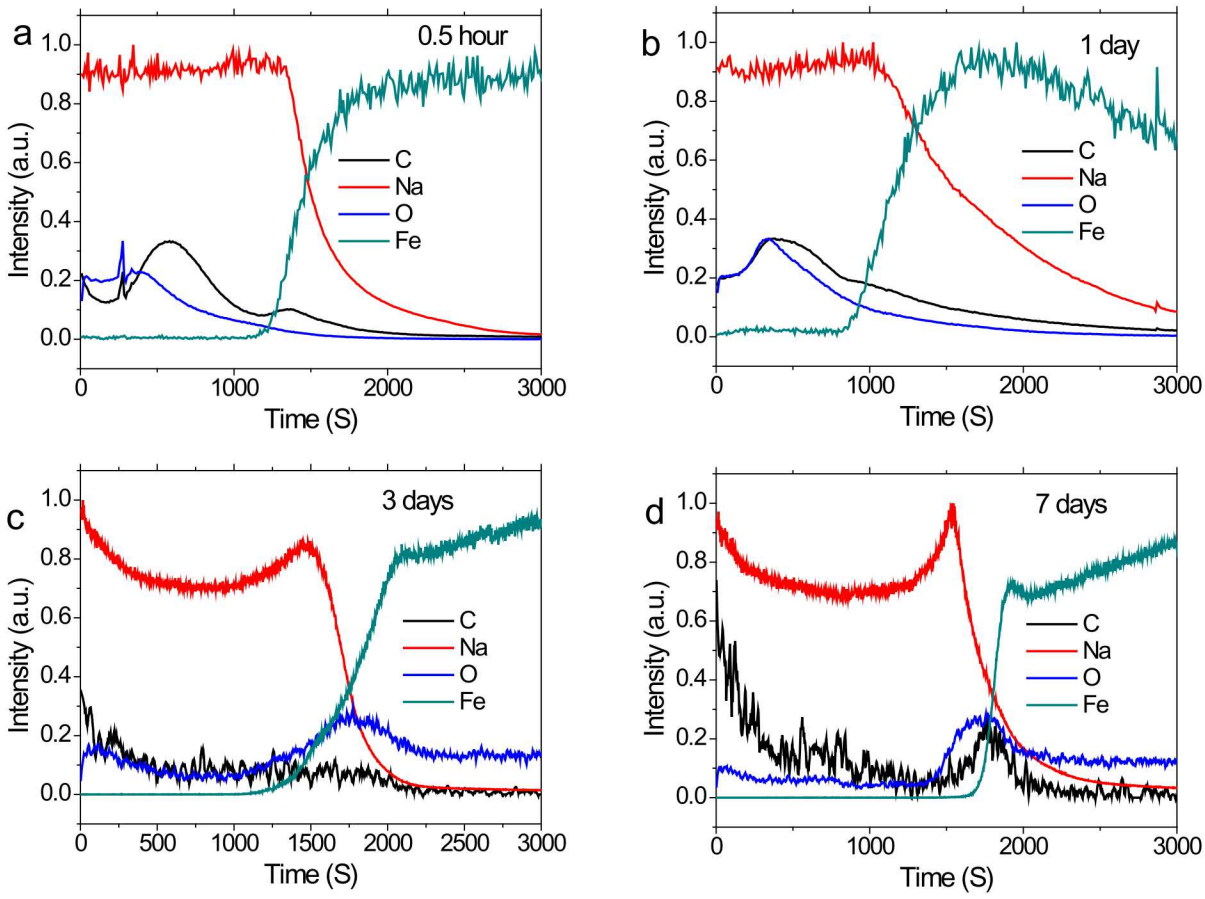

Figure S7: TOF-SIMS depth profiles across the fully sodiated 100nmSb specimens after being stored at ambient for 0.5 hours, 1, 3 and 7 days.